

# Photon-mediated charge-exchange reactions between $^{39}\text{K}$ atoms and $^{40}\text{Ca}^+$ ions in a hybrid trap

Hui Li,<sup>1</sup> S. Jyothi,<sup>2</sup> Ming Li,<sup>1</sup> Jacek Kłos,<sup>1,3</sup> Alexander Petrov,<sup>1,4</sup> Kenneth R Brown,<sup>2</sup> and Svetlana Kotochigova<sup>1,\*</sup>

<sup>1</sup>*Department of Physics, Temple University, Philadelphia, Pennsylvania 19122, USA*

<sup>2</sup>*Department of Electrical and Computer Engineering,  
Duke University, Durham, North Carolina 27708, USA*

<sup>3</sup>*Department of Chemistry and Biochemistry, University of Maryland, College Park, Maryland 20742, USA*

<sup>4</sup>*NRC, Kurchatov Institute PNPI, Gatchina, 188300, and Division of Quantum Mechanics,  
St. Petersburg State University, St. Petersburg, 199034, Russia*

(Dated: December 21, 2024)

We present experimental evidence of charge exchange between laser-cooled potassium  $^{39}\text{K}$  atoms and calcium  $^{40}\text{Ca}^+$  ions in a hybrid atom-ion trap and give quantitative theoretical explanations for the observations. The  $^{39}\text{K}$  atoms and  $^{40}\text{Ca}^+$  ions are held in a magneto-optical (MOT) and a linear Paul trap, respectively. Fluorescence detection and high resolution time of flight mass spectra for both species are used to determine the remaining number of  $^{40}\text{Ca}^+$  ions, the increasing number of  $^{39}\text{K}^+$  ions, and  $^{39}\text{K}$  number density as functions of time. Simultaneous trap operation is guaranteed by alternating periods of MOT and  $^{40}\text{Ca}^+$  cooling lights, thus avoiding direct ionization of  $^{39}\text{K}$  by the  $^{40}\text{Ca}^+$  cooling light. We show that the K-Ca $^+$  charge-exchange rate coefficient increases linearly from zero with  $^{39}\text{K}$  number density and, surprisingly, the fraction of  $^{40}\text{Ca}^+$  ions in the  $4\text{p}^2\text{P}_{1/2}$  electronically-excited state. Combined with our theoretical analysis, we conclude that these data can only be explained by a process that starts with a potassium atom in its electronic ground state and a calcium ion in its excited  $4\text{p}^2\text{P}_{1/2}$  state producing ground-state  $^{39}\text{K}^+$  ions and metastable, neutral Ca ( $3\text{d}4\text{p}^3\text{P}_1$ ) atoms, releasing only  $150\text{ cm}^{-1}$  equivalent relative kinetic energy. Charge-exchange between either ground- or excited-state  $^{39}\text{K}$  and ground-state  $^{40}\text{Ca}^+$  is negligibly small as no energetically-favorable product states are available. Our experimental and theoretical rate coefficients are in agreement given the uncertainty budgets.

## I. INTRODUCTION

Over the past few decades, laser cooling and trapping of atoms, ions, and molecules have significantly contributed to advancing fundamental atomic, molecular, and optical physics research. More recently, experiments successfully merged ion and neutral atom trapping techniques. These experiments include the study of reaction dynamics of neutral atoms and atomic ions [1–16], as well as of cold atoms and molecular ions[17–19]. Here, the long storage times of laser-cooled ion-atom systems has allowed the study of processes that are difficult to observe otherwise. The internal and external states of the atoms and ions can be manipulated using laser fields, which enables a carefully investigation of the quantum-state dependence of a process.

Most research has focused on colliding neutral and ionic atoms or molecules prepared in their electronic ground state. When one or both colliding partners, however, are prepared in excited electronic states more inelastic channels become available and richer dynamics occurs with corresponding challenges in the theoretical interpretation. Recently, such inelastic collisions have been reported for the ion in an excited state [4, 12, 15, 20–22], for an excited atom colliding with an ion or a charged molecule [15, 23–26], and for both in excited states [15].

Ions are optically excited to metastable states in such applications as optical frequency standards, quantum simulation, quantum computing and astronomy [27–31], making their collisional properties highly relevant. Finally, while many of the experiments share common features and theoretical models that explain their results, different atomic and/or ionic species have unique experimental and theoretical details that are well worth documenting.

In this article, we present the theoretical and experimental investigation of cold charge-exchange collisions between laser-cooled potassium ( $^{39}\text{K}$ ) and calcium ( $^{40}\text{Ca}^+$ ) ions. The nearly-equal masses of potassium and calcium enables the simultaneous trapping of the reactant and resultant ions in the same ion trap. Further, direct detection of the ions using a high-resolution time-of-flight mass spectrometer (TOFMS) allows us to follow charge exchange as a function of time. We also show that our data are explained by a process that starts with a potassium atom in its electronic ground state and a calcium ion in its excited  $4\text{p}^2\text{P}_{1/2}$  state producing ground-state  $^{39}\text{K}^+$  ions and metastable, neutral Ca ( $4\text{s}4\text{p}^3\text{P}_1$ ) atoms, releasing only  $150\text{ cm}^{-1}$  equivalent relative kinetic energy. Our measured charge-exchange rate coefficient is in good agreement with the theoretical estimate.

The article is organized as follows. In section II, we describe the experimental setup and measurements of the charge-exchange rate coefficient. The theoretical models for different charge exchange pathways are detailed in section III, followed by a discussion in section IV. Details of our theoretical methods are described in section V.

\* skotoch@temple.edu

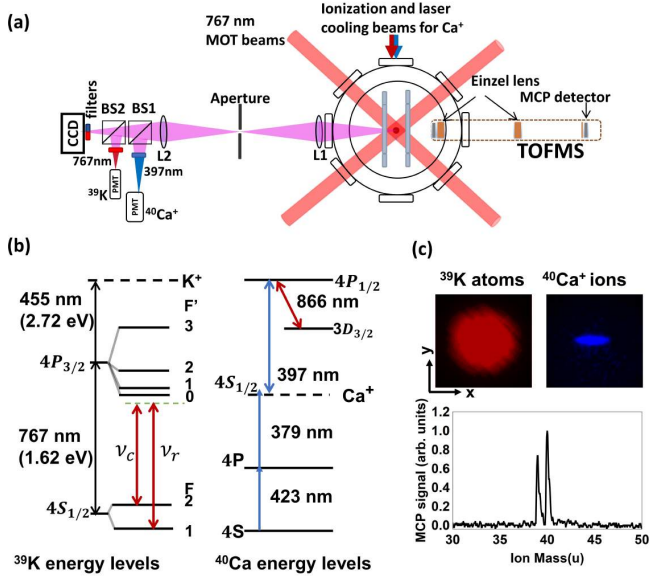


FIG. 1. (a) Top view of the experimental apparatus illustrating laser setups, fluorescence detection, and ion time of flight detection. (b) the relevant states, energy levels, and laser colors (not to scale) of  $^{39}\text{K}$ ,  $^{39}\text{K}^+$ ,  $^{40}\text{Ca}$ , and  $^{40}\text{Ca}^+$ . Red vertical lines with arrows and labels  $v_c$  and  $v_r$  correspond to the cooling and repumper lasers for  $^{39}\text{K}$ , respectively. The four lasers (blue and red lines with arrows) that control neutral  $^{40}\text{Ca}$  and ionic  $^{40}\text{Ca}^+$  are discussed in the text. (c) CCD images of the  $^{39}\text{K}$  MOT and  $^{40}\text{Ca}^+$  ions, and a TOF mass spectrum showing both  $^{39}\text{K}^+$  and  $^{40}\text{Ca}^+$  ion peaks.

## II. EXPERIMENTAL SETUP AND OBSERVATIONS

The experiments are performed in a spatially overlapped ion-atom hybrid trap comprised of a magneto optical trap (MOT) for neutral  $^{39}\text{K}$  atoms and a linear Paul trap for  $^{40}\text{Ca}^+$  ions [32]. A schematic of the experimental setup is shown in Fig. 1(a). The ion trap is a segmented electrode linear quadrupole trap with four central rf electrodes (driven at 1.7 MHz) for radial trapping and eight end cap dc electrodes for axial trapping. The apparatus is integrated with a high-resolution TOFMS consisting of two Einzel lenses for ion collimation and a microchannel plate for ion detection. The ions are radially extracted from the Paul trap towards the detector by turning off the rf voltages while, simultaneously, applying high dc voltages on the central electrodes to create a potential gradient.

Neutral  $^{39}\text{K}$  atoms derived from a potassium ampule are cooled and trapped in a MOT using three mutually orthogonal and retro-reflected laser beams. The energy-level diagram of  $^{39}\text{K}$  atoms relevant for our experiments is shown in Fig. 1(b). Cooling and repumper beams are derived from the same 767 nm laser by MOGLabs locked to the D2 crossover peak of a saturation absorption spectrum. A pair of acousto-optic modulators (AOMs) are used to set the desired detunings for the cooling (20 MHz

to the red of the  $4s(F = 2)$  to  $4p(F = 3)$  transition) and repumper (20 MHz to the red of the  $F = 1$  to  $F = 3$  transition) beams. The quadrupole magnetic field for the MOT is created by a pair of coils in anti-Helmholtz configuration mounted outside the vacuum chamber.

Neutral calcium atoms are produced by heating a calcium dispenser with a current of about 2.7 A. The  $^{40}\text{Ca}$  atoms are ionized by two-photon ionization using lasers at wavelengths of 423 nm and 379 nm focused at the center of the ion trap. The  $^{40}\text{Ca}^+$  ions are Doppler cooled using a 397 nm laser and repumped with an 866 nm laser. The relevant states and energy levels of  $^{40}\text{Ca}$  and  $^{40}\text{Ca}^+$  are shown in Fig. 1(b). All laser beams for  $^{40}\text{Ca}^+$  are derived from a multi-diode laser module from Toptica Photonics.

To study cold interactions between  $^{39}\text{K}$  and  $^{40}\text{Ca}^+$ , the centers of the MOT and Paul trap must coincide. Optimization of the trap overlap is achieved by either moving the MOT center by changing the currents through the coil pair or by moving the center of the Paul trap by changing the dc voltages on the ion trap electrodes. The quality of the relative positioning of the trap centers has been presented in detail in [32]. For stable co-trapping and cooling of  $^{39}\text{K}$  and  $^{40}\text{Ca}^+$ , the 767 nm and 397 nm laser beams are alternately switched at a frequency of 2 kHz using AOMs [32]. This prevents ionization of potassium atoms in the MOT from the  $4P_{3/2}$  state by the 397 nm  $\text{Ca}^+$  cooling laser beam and limits the reactants collision channels to  $\text{K}(\text{S})+\text{Ca}^+(\text{P})$ ,  $\text{K}(\text{P})+\text{Ca}^+(\text{S})$ , and  $\text{K}(\text{S})+\text{Ca}^+(\text{S})$ .

Fluorescence from  $^{39}\text{K}$  and  $^{40}\text{Ca}^+$  is detected using photo multiplier tubes (PMT) and an EM-CCD camera. The  $^{39}\text{K}$  number density is determined from the fluorescence signal. Ions are also detected using TOFMS, enabling the direct observation of non-fluorescing reaction products such as the  $^{39}\text{K}^+$  ions. With the optimal extraction voltages, a mass resolution  $m/\Delta m$  of 208 is achieved, which is sufficient to resolve the  $^{40}\text{Ca}^+$  and  $^{39}\text{K}^+$  ion peaks. EMCCD images of  $^{39}\text{K}$  and  $^{40}\text{Ca}^+$  ions as well as a representative TOF mass spectrum of  $^{39}\text{K}^+$  and  $^{40}\text{Ca}^+$  ions are shown in Fig. 1(c).

The experiment is controlled by a Kasli FPGA and programmed using ARTIQ (Advanced Real-Time Infrastructure for Quantum physics) [32, 33] provided by m-labs. A typical experimental sequence to measure  $^{39}\text{K}$ - $^{40}\text{Ca}^+$  charge exchange is shown in Fig. 2. First, we load and cool approximately 1000  $^{40}\text{Ca}^+$  into the ion trap. The photo-ionizing lasers for calcium are then blocked using a mechanical shutter to avoid ionization of  $^{39}\text{K}$  atoms by these lasers. The MOT laser beams are now turned on to load the MOT to saturation. While loading the MOT, currents on an additional pair of magnetic coils in Helmholtz configuration are turned on to shift the MOT magnetic-field center a few mm from the center of the ion trap. This avoids any interaction between  $^{39}\text{K}$  and  $^{40}\text{Ca}^+$  during the MOT loading process. The MOT center is then moved back to the ion-trap center by turning off the Helmholtz coil current. The  $^{39}\text{K}$  atoms

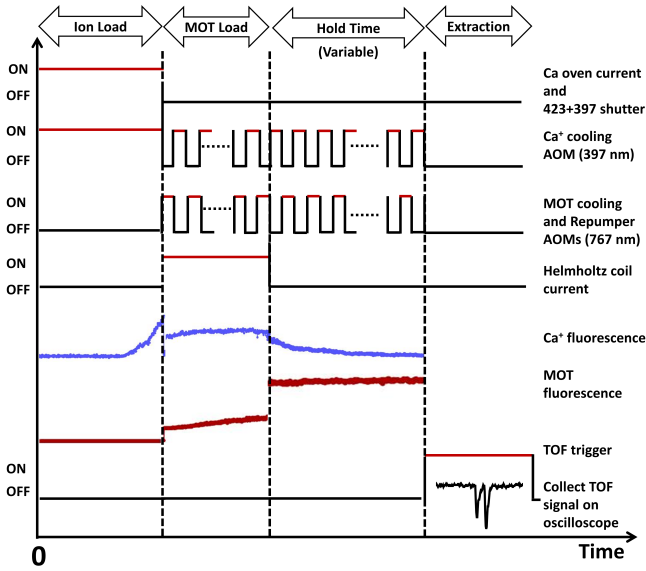


FIG. 2. Experimental control sequence to measure the charge-exchange rate between  $^{39}\text{K}$  and  $^{40}\text{Ca}^+$  as described in the text. Since the 767 nm and 397 nm laser beams are never simultaneously turned on, excited  $^{39}\text{K}$  and excited  $^{40}\text{Ca}^+$  are not simultaneously present. Consequently, charge-exchange collisions only occur via the  $\text{K}(\text{S})+\text{Ca}^+(\text{P})$ ,  $\text{K}(\text{P})+\text{Ca}^+(\text{S})$ , and  $\text{K}(\text{S})+\text{Ca}^+(\text{S})$  channels.

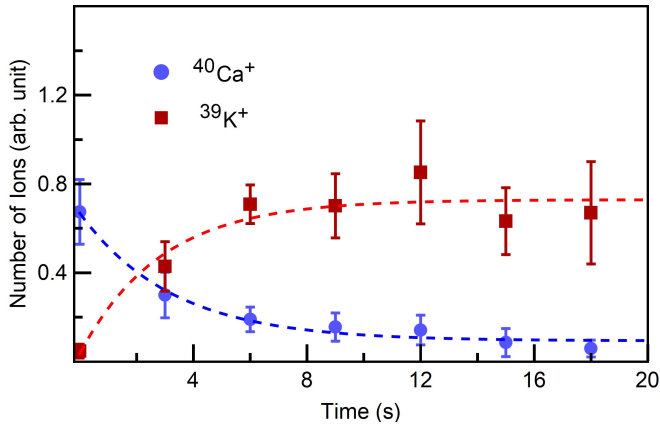


FIG. 3. The number of  $^{40}\text{Ca}^+$  and  $^{39}\text{K}^+$  ions as functions of time for which the two species are held together. Error bars are one standard deviation uncertainties based on six measurements. Dashed lines are exponential fits to the data. The  $^{39}\text{K}$  number density in the MOT is  $10^9$  atoms/cm $^3$ .

and  $^{40}\text{Ca}^+$  ions are then allowed to interact for different hold times. During the hold time, the 767 nm and 397 nm laser beams are never on at the same time.

The TOFMS signal, collected as a function of hold time, provides evidence of charge exchange, because our Paul trap holds  $^{40}\text{Ca}^+$  and  $^{39}\text{K}^+$  ions equally well due to their comparable masses. That is, product  $^{39}\text{K}^+$  ions are trapped and can be detected with TOFMS. Figure 3 shows the detected number of  $^{40}\text{Ca}^+$  and  $^{39}\text{K}^+$  ions as

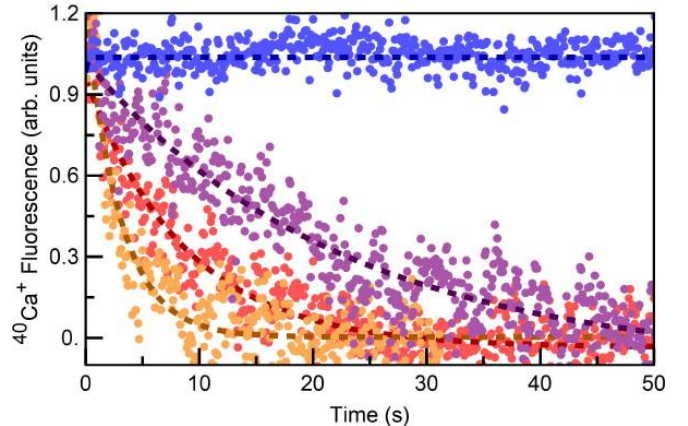


FIG. 4. Typical fluorescence data from  $^{40}\text{Ca}^+$  ions as functions of time in the absence and presence of  $^{39}\text{K}$  atoms in the MOT. Blue circles correspond to  $^{40}\text{Ca}^+$  fluorescence data in the absence of the neutral atoms. Purple, red and orange circles show  $^{40}\text{Ca}^+$  fluorescence when the ions are held together with  $^{39}\text{K}$  atoms for increasing  $^{39}\text{K}$  number density, respectively. Dashed lines are exponential fits to the data.

a function of hold time. The number of  $^{40}\text{Ca}^+$  decreases with time with a simultaneous one-to-one increase in the number of  $^{39}\text{K}^+$  ions.

Figure 4 shows typical  $^{40}\text{Ca}^+$  fluorescence as a function of hold time in the absence and presence of  $^{39}\text{K}$  atoms. Without  $^{39}\text{K}$  atoms, the number of trapped, laser-cooled  $^{40}\text{Ca}^+$  ions is constant for several minutes. When  $^{40}\text{Ca}^+$  ions are allowed to interact with  $^{39}\text{K}$  atoms, however, the  $^{40}\text{Ca}^+$  ions disappear in a few seconds as a result of charge exchange. Decay rates measured by  $^{40}\text{Ca}^+$  fluorescence and TOFMS data are consistent. As TOFMS is destructive, both ion and atom traps need to be reloaded for each hold time. Hence, for most measurements described in this article  $^{40}\text{Ca}^+$  ion fluorescence is used to measure decay rates. In fact, fluorescence has been the preferred measurement tool of ultra-cold chemical reaction rates [1, 4, 5, 34].

Figure 5 shows the rate of charge exchange as a function of  $^{39}\text{K}$  number density in a MOT when the fraction of  $^{40}\text{Ca}^+$  ions in the excited  $^2\text{P}_{1/2}$  state is 0.4. This excited-state fraction is controlled by the frequency detuning of the 397-nm  $^{40}\text{Ca}^+$  cooling laser from the  $4\text{S}$  to  $4\text{P}_{1/2}$  transition. The rate coefficient increases with  $^{39}\text{K}$  number density and a linear fit assuming no charge exchange at zero  $^{39}\text{K}$  number density gives a rate coefficient of  $(4.0 \pm 0.2) \times 10^{-10}$  cm $^3$ /s.

To examine the effect of the excited electronic state of  $^{40}\text{Ca}^+$  ions on charge exchange, we varied the population in the  $4\text{P}_{1/2}$  state by adjusting the frequency detuning of the  $^{40}\text{Ca}^+$  cooling laser. Figure 6 shows these data. The rate coefficients increases linearly with excited-state population. Hence, we conclude that when all  $^{40}\text{Ca}^+$  ions are in the electronic ground state the charge-exchange rate coefficient is small, or more-precisely falls below our detection threshold. When all  $^{40}\text{Ca}^+$  ions are in the ex-

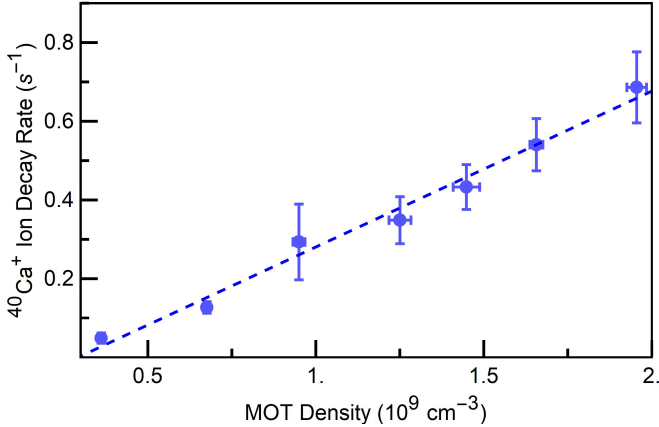


FIG. 5. Loss rate of  ${}^{40}\text{Ca}^+$  ions in the presence of its 397-nm cooling light as a function of  ${}^{39}\text{K}$  number density in the MOT. A linear fit to the data assuming no charge exchange when there are no  ${}^{39}\text{K}$  atoms present gives a rate coefficient of  $(4.0 \pm 0.2) \times 10^{-10} \text{ cm}^3/\text{s}$ . The detuning of the 397-nm laser that cools  ${}^{40}\text{Ca}^+$  is such that the excited-state  ${}^{40}\text{Ca}^+(2\text{P}_{1/2})$  population is 0.4.

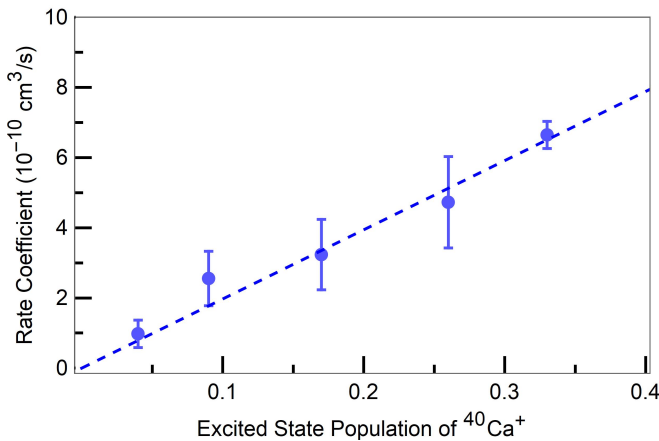


FIG. 6. Charge-exchange rate coefficient as a function of the  ${}^{40}\text{Ca}^+(4\text{P}_{1/2})$  excited-state population. The error bars are one standard deviation uncertainties based on ten measurements.

cited  $4\text{p}^2\text{P}_{1/2}$  state the rate coefficient approaches  $10^{-9} \text{ cm}^{-3}/\text{s}$ .

### III. THEORETICAL MODELS FOR THE CHARGE-EXCHANGE REACTION

#### A. Charge exchange in the presence of the $\text{Ca}^+$ ion cooling laser

Our experimental measurements provide clear evidence of the important role that the excitation of  ${}^{40}\text{Ca}^+$  ions into the  $4\text{p}^2\text{P}_{1/2}$  state plays in changing the charge exchange rate. To better understand the reaction mecha-

nism we theoretically studied the excited-state electronic potentials of the  $\text{KCa}^+$  molecule in order to identify processes that lead to high-yield reaction channels and the formation of  $\text{K}^+$  ions as well as neutral excited-state Ca atoms.

Enhanced collisional charge-exchange rate occurs when molecular energy levels of  $\text{Ca}^+\text{K}$  and  $\text{K}^+\text{Ca}$  configurations are energetically close allowing for efficient charge exchange. As shown in Fig. 7 we find such conditions in collisional interactions between ground state  $\text{K}(2\text{S}_{1/2})$  atoms and electronically-excited  $\text{Ca}^+(2\text{P}_{j=1/2})$  ions on the one hand and between ground state  $\text{K}^+(1\text{S}_0)$  ions and metastable  $\text{Ca}(3\text{d}4\text{p}^3\text{P}_{j=1})$  atoms on the other. These two dissociation limits are only separated by  $150 \text{ cm}^{-1}$  energy equivalent and have energies lying approximately  $E/\hbar c = 25000 \text{ cm}^{-1}$  above the  $\text{K}(4\text{s}^2\text{S}_{1/2}) + \text{Ca}^+(2\text{S}_{1/2})$  ground state. This latter energy corresponds to a photon with a wavelength of 397 nm, the wavelength of the cooling laser for the  $\text{Ca}^+$  ion. Figure 7b) also shows that potentials dissociating to the two nearly-degenerate dissociation limits have an avoided crossing near  $28a_0$  leading to significant charge exchange.

Figure 7 is based on an implicit approximation for our coordinate system that will be used throughout this paper. In charge exchange an electron moves from one atom to another, thereby, changing the center of charge and mass of the dimer. We assume that the effects of these changes on rate coefficients is negligible and express all molecular interactions in terms of separation  $\vec{R} = (R, \theta, \varphi)$  in spherical coordinates defined as the distance  $R$  between and orientation  $\theta, \varphi$  of the center of mass of neutral  ${}^{39}\text{K}$  with respect to that of the center of mass of ionic  ${}^{40}\text{Ca}^+$  in a laboratory-fixed coordinate frame. The reduced mass  $\mu = m_{\text{K}}m_{\text{Ca}}/(m_{\text{K}} + m_{\text{Ca}})$  is that of the  ${}^{39}\text{K} + {}^{40}\text{Ca}^+$  system, where  $m_{\text{K}}$  and  $m_{\text{Ca}}$  are the masses of  ${}^{39}\text{K}$  and  ${}^{40}\text{Ca}^+$ , respectively.

Four interaction terms are important for the reaction between our atoms and ions. These are the asymptotic splittings of the relevant configurations, their long-range molecular interaction potentials, and the charge-state changing couplings. Finally, we must include molecular rotation. Atomic and ionic energies have been taken from Ref. [35], including the relativistic spin-orbit splittings among  $\text{Ca}^+(4\text{p}^2\text{P}_{j=1/2,3/2})$  and  $\text{Ca}(3\text{d}4\text{p}^3\text{P}_{j=0,1,2})$ . The molecular interactions have two contributions: a) an anisotropic  $C_4/R^4$  induction interaction between the charge of the ion and the induced dipole moment of the neutral atom and b) an anisotropic  $C_3/R^3$  interaction between the ion charge and the quadrupole moment of an excited neutral atom. Both  $C_4$  and  $C_3$  coefficients depend on the orientation of  $\vec{R}$  and only depend on properties of the neutral atom. Dispersive van-der-Waals potentials do not contribute significantly for  $R > 20a_0$ .

If we ignore the rotation of the molecule for the moment, a convenient basis for the reaction from  $\text{K}(4\text{s}^2\text{S}_{j_a}) + \text{Ca}^+(4\text{p}^2\text{P}_{j_b})$  to  $\text{K}^+(1\text{S}_{j_a'}) + \text{Ca}(3\text{d}4\text{p}^3\text{P}_{j_b'})$

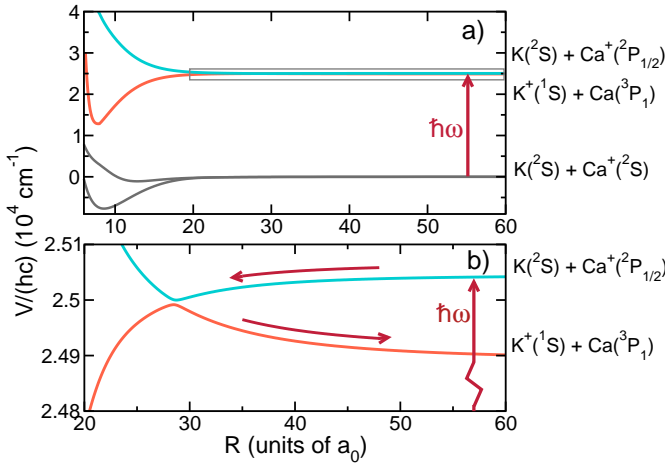


FIG. 7. a) Schematic of the relevant electronic potential energy curves as functions of the  $K+Ca^+$  separation  $R$ . Only curves relevant for charge-exchange starting from the absorption of a photon from the  $K(2^2S_{1/2})+Ca^+(2^2S_{1/2})$  to  $K(2^2S_{1/2})+Ca^+(2^2P_{1/2})$  the channels are shown. From low to high energy the two potentials dissociating to the  $K(2^2S_{1/2})+Ca^+(2^2S_{1/2})$  limit have  $^1\Sigma^+$  and  $^3\Sigma^+$  symmetry, respectively. The zero of energy is at the  $K(2^2S_{1/2})+Ca^+(2^2S_{1/2})$  dissociation limit and  $a_0$  is the Bohr radius. Panel b) zooms in on the potentials leading to charge exchange to  $K^+(1^1S_{1/2})+Ca(3^3P_1)$  releasing only  $150\text{ cm}^{-1}$  equivalent kinetic energy. The gray box in panel a) corresponds to the energy and separation region shown in panel b).

is the body-fixed product basis

$$|q_a, j_a, \Omega_a\rangle |q_b, j_b, \Omega_b\rangle, \quad (1)$$

where  $q_i = 0, +1$  is charge state of the atom or ion  $i = a$  and  $b$  for  $K/K^+$  and  $Ca/Ca^+$ , respectively, and  $\Omega_i$  is the projection quantum number of the total atomic/ionic angular momentum  $\vec{j}_i$  along the interatomic axis  $\vec{R}$ . We use that within the context of this charge-exchange process labels  $q_i$ ,  $j_i$ , and  $\Omega_i$  uniquely specify an atomic/ionic state. A list of states in found in Table I.

The asymptotic splittings are diagonal in the product basis of Eq. 1. The matrix elements of the two long-range molecular interactions are diagonal in and independent of the quantum numbers of the ion and only depend on the state of the neutral atom. In fact,

$$\frac{\langle 0, j_s, \Omega_s | C_3 | 0, j'_s, \Omega'_s \rangle}{R^3} = \delta_{\Omega_s \Omega'_s} \frac{q}{R^3} (-1)^{j_s - \Omega_s} \times \begin{pmatrix} j_s & 2 & j'_s \\ -\Omega_s & 0 & \Omega_s \end{pmatrix} \langle j_s || Q_2 || j'_s \rangle$$

in atomic units for the neutral atom with quantum numbers  $j_s \Omega_s$  [16]. Here,  $q = +1$  for the corresponding ion,  $\delta_{\Omega \Omega'}$  is the Kronecker delta, and  $(::)$  denotes a Wigner 3-j symbol. The matrix elements of the induction potential for  $K(4s^2S)$  are

$$\frac{\langle 0, j_s, \Omega_s | C_4 | 0, j'_s, \Omega'_s \rangle}{R^4} = -\delta_{j_s \Omega_s, j'_s \Omega'_s} \frac{q^2}{2R^4} \alpha_{0,s},$$

TABLE I. The quantum numbers for our body-fixed basis states for the  $K(4s^2S_{j_a}) + Ca^+(4p^2P_{j_b})$  to  $K^+(1^1S_{j'_a}) + Ca(3d4p^3P_{j'_b})$  reaction and the corresponding diagonal  $C_3$  and  $C_4$  coefficients in atomic units. Channels are uniquely described by the charge  $q_i$ , atomic angular momenta  $j_i$ , and its body-fixed projection  $\Omega_i$  on the internuclear axis with  $i = a$  and  $b$  for  $K$  and  $Ca$ , respectively. Potentials are degenerate for  $-\Omega$  and  $\Omega$ , where  $\Omega = \Omega_a + \Omega_b$ .

K or $K^+$			Ca or $Ca^+$			$C_3$	$C_4$
$q_a$	$j_a$	$\Omega_a$	$q_b$	$j_b$	$\Omega_b$		
0	1/2	1/2	+1	1/2	-1/2	0	-145.29
0	1/2	-1/2	+1	1/2	1/2	0	-145.29
0	1/2	1/2	+1	1/2	1/2	0	-145.29
+1	0	0	0	0	0	0	-641.0
+1	0	0	0	1	0	5.874	97.95
+1	0	0	0	1	1	-2.937	-1015.5
+1	0	0	0	2	0	-5.874	-1404.7
+1	0	0	0	2	1	-2.937	-1027.9
+1	0	0	0	2	2	5.874	102.7

while the diagonal matrix elements of the induction potential for  $Ca(3d4p^2P)$  states are

$$\langle 0, j_s, \Omega_s | C_4 | 0, j_s, \Omega_s \rangle = -\frac{q^2}{2R^4} \left[ \alpha_{0,s} + \alpha_{2,s} \frac{3\Omega_s^2 - j_s(j_s + 1)}{j_s(2j_s - 1)} \right],$$

from Ref. [36]. Off-diagonal matrix elements, coupling states with  $|\Delta j_s| \leq 2$ , can also be found in Ref. [36]. Finally,  $\langle j_s || Q_2 || j_s \rangle$ ,  $\alpha_{0,s}$ , and  $\alpha_{2,s}$  are the reduced quadrupole-moment matrix elements and static scalar and tensor polarizabilities of the neutral atom  $s$  with angular momentum  $j_s$ , respectively. The sum  $\Omega = \Omega_a + \Omega_b$  is conserved for both interactions.

We have calculated the reduced matrix element of the quadrupole moment of  $Ca(3d4p^3P)$  states using a non-relativistic multi-configuration-interaction method with an all-electron correlation-consistent polarized valence-only quintuple zeta (CC-pV5Z) basis set [37]. For the triplet states calculations have been performed in the  $B_{3u}$  representation. Then the calculations provide the expectation value of the quadrupole operator  $\hat{Q}_{20}$  for state  $|0, j_s = 1, \Omega_s = 0\rangle$  of neutral  $Ca(3d4p^3P)$ . The value is  $-11.748$  a.u. with an one-standard-deviation uncertainty of  $3.0$  a.u. (Here, a.u. is an abbreviation for atomic unit and we keep all digits to avoid roundoff problems.) Of course, the quadrupole moment for an S state is zero.

We used the static scalar polarizability of  $290.48$  a.u. for  $K(4s^2S_{1/2})$  from Ref. [38]. For  $Ca(3d4p^3P_{0,1,2})$  states we have computed  $\alpha_{0,s}$  and  $\alpha_{2,s}$  using transition dipole moments from [39] and perturbation theory. Values for quadrupole moments and static polarizabilities are summarized in Table II. Table I lists the diagonal  $C_3$  and  $C_4$  coefficients for the relevant channels  $|q_a, j_a \Omega_a\rangle |q_b, j_b \Omega_b\rangle$ .

The charge-exchange-inducing coupling between the body-fixed channels is computed based on the application of the Heitler-London method, in which the electron

TABLE II. Atomic parameters in atomic units used to generate the interaction potentials. See text for definitions.

Term	$\alpha_0$	$\alpha_2$	$\langle j  Q_2  j\rangle$
K (4s)	$^2S_{1/2}$	290.58	
Ca (4s <sup>2</sup> )	$^1S_0$	157.1	
Ca (3d4p)	$^3P_0$	1282.0	
Ca (3d4p)	$^3P_1$	1288.7	742.3 -16.086
Ca (3d4p)	$^3P_2$	1302.0	-1507.4 32.173

in the 4s orbital of K moves to the unoccupied 3d orbital of Ca<sup>+</sup>. The coupling is then given by the overlap integral of these non-relativistic atomic Hartree-Fock orbitals and the electron-nucleus Coulomb interaction potential. The coupling matrix element between channels  $|0, j_a \Omega_a\rangle |+1, j_b \Omega_b\rangle$  and  $|+1, j'_a \Omega'_a\rangle |0, j'_b \Omega'_b\rangle$  with the same  $\Omega = \Omega_a + \Omega_b = \Omega'_a + \Omega'_b = 0$ , 1 are  $\sqrt{\frac{2}{30}}O(R)$  and  $\sqrt{\frac{1}{30}}O(R)$ , respectively, where

$$O(R) = \int d^3r \phi_{K,4s}(\vec{r} - \vec{r}_K) \frac{e^2}{4\pi\epsilon_0} \left[ \frac{1}{|\vec{r} - \vec{r}_K|} + \frac{1}{|\vec{r} - \vec{r}_{Ca}|} \right] \times \phi_{Ca,3d}(\vec{r} - \vec{r}_{Ca}), \quad (2)$$

$\phi_{K,4s}(\vec{r} - \vec{r}_K)$  and  $\phi_{Ca,3d}(\vec{r} - \vec{r}_{Ca})$  are the spatial-components of the K(4s) and Ca(3d) Hartree-Fock electron orbitals, respectively, and  $\vec{r}_i$  is the location of nucleus  $i = K$  or Ca. For our choice of coordinate system  $R = |\vec{r}_K - \vec{r}_{Ca}|$  to good approximation. The function  $O(R)$  is  $hc \times 5.6 \text{ cm}^{-1}$  at  $R = 28a_0$  and rapidly goes to zero for  $R \rightarrow \infty$ .

Figure 8 shows three views of the long-range adiabatic  $\Omega = 0^\pm$ , 1 and 2 potentials for the excited-state charge-exchange reaction. Panels a) and c) have been found by diagonalizing the potential matrix at each  $R$  in the body-fixed basis of Eq. 1 without the charge-exchange-inducing coupling, while in panel b) this coupling has been included. Consequently, curves dissociating to the K(4s  $^2S_{1/2}$ ) + Ca<sup>+</sup>(4p  $^2P$ ) limits in Fig. 8a) cross those dissociating to the K<sup>+</sup>( $^1S_0$ ) + Ca(3d4p  $^3P$ ) limits. These crossings become avoided crossings once charge-exchange-inducing couplings are included, as shown in Fig. 8b) around  $R = 28a_0$ . The (avoided) crossings for the curves dissociating to the K(4s  $^2S_{1/2}$ ) + Ca<sup>+</sup>(4p  $^2P_{3/2}$ ) limits are not energetically-accessible from our K(4s  $^2S_{1/2}$ ) + Ca<sup>+</sup>(4p  $^2P_{1/2}$ ) entrance channels and need not be considered further. Charge exchange can only occur between states with the same  $\Omega$ , which in our system only occurs between  $\Omega = 0^\pm$  and 1 potentials. The asymptotic splittings between the entrance channel and the exit channels is approximately  $hc \times 150 \text{ cm}^{-1}$ .

For the experimental temperature near 0.1 K and a long-range induction potential, the number of partial waves or relative orbital angular momenta of the atom-ion system,  $\vec{\ell}$ , contributing to the charge-exchange rate coefficient is large. Then we are justified in ap-

proximating the rotational Hamiltonian of the diatom and use the infinite-order sudden approximation [40]. This corresponds to performing coupled-channels calculations for each triple  $J$ ,  $M$ , and  $\Omega$  in the channel basis  $\sqrt{(2J+1)/8\pi^2}D_{M\Omega}^{J*}(\varphi, \theta, 0)|q_a, j_a \Omega_a\rangle |q_b, j_b \Omega_b\rangle$  ignoring couplings between different  $\Omega^\pm$  and using a diagonal centrifugal potential with matrix element  $\hbar^2 J(J+1)/2\mu R^2$  for each channel independent of  $M$  and  $\Omega^\pm$ . Here,  $D_{mm'}^{j'}(\alpha\beta\gamma)$  is a Wigner rotation matrix,  $\Omega = \Omega_a + \Omega_b$ ,  $\vec{J} = \vec{j}_a + \vec{j}_b + \vec{\ell}$  is the total molecular angular momentum with projection quantum number  $M$ . For  $\Omega = 0^-$ ,  $0^+$ , and 1 channels are coupled for each  $J$  and  $M$ , respectively, as we can ignore the effects of the energetically-closed K(4s  $^2S_{1/2}$ ) + Ca<sup>+</sup>(4p  $^2P_{3/2}$ ) channels. For a valid coupled-channels calculation we extend the potentials to  $R \rightarrow 0^+$   $a_0$  to have a repulsive inner wall by adding repulsive  $C_{12}/R^{12}$  potentials to the diagonal potential matrix elements in the channel states. Typical examples can be seen in Fig. 7.)

We propagate the wavefunctions in the coupled-channels calculations for each  $J, M, \Omega^\pm$  using Gordon's propagator [41] and match to scattering boundary conditions at large  $R$  to obtain partial charge-exchange rate coefficients  $K_{JM, \Omega^\pm}(E)$ , where  $E$  is the entrance-channel collision energy and have summed over all exit channels.

$$K(E) = \sum_{\Omega^\pm=0^+, 0^-, 1} g_{\Omega^\pm} \sum_{J=0}^{\infty} (2J+1) K_{JM, \Omega^\pm}(E), \quad (3)$$

where  $g_{0^+} = 1/4$ ,  $g_{0^-} = 1/4$ , and  $g_1 = 1/2$ . Finally, we thermally average assuming a Gaussian distribution with a temperature  $T_K$  and  $T_{Ca}$  for  $^{39}\text{K}$  and  $^{40}\text{Ca}^+$ , respectively. The thermalized total rate coefficient then only depends on the effective temperature

$$T_{\text{eff}} = \frac{m_K T_{Ca} + m_{Ca} T_K}{M} \approx \frac{m_K}{M} T_{Ca}.$$

where  $M = m_K + m_{Ca}$  and the second approximate equality follows from  $T_K \ll T_{Ca}$  in our experiments. Figure 9 shows results for the total charge-exchange rate coefficient from our coupled-channels calculations and compares them to our measurement at  $T_{\text{eff}} = 0.2$  K. The figure first shows a rate coefficient as a function of collision energy  $E$ . The rate coefficient has many peaks resulting from shape resonances contained by the barrier created by the attractive induction potential and the repulsive centrifugal potential. At  $E/k < 0.2$  K already twelve such resonances can be observed. Here,  $k$  is the Boltzmann constant. In fact, for  $E/k = 0.2$  K at least forty  $J$  contribute significantly to the total charge-exchange rate coefficient. Once the rate coefficient is thermally-averaged the peaks smooth out and the rate coefficient is a slowly increasing function with  $T_{\text{eff}}$  for  $T_{\text{eff}} < 1$  K. Finally, we have studied the effects of changing the quadrupole moment and thus the  $C_3$  coefficient within its 20% uncertainty on the thermalized rate coefficient. As shown in Fig. 9 we observe that the rate coefficient changes by 10% to 20% for temperatures between 0.01 K

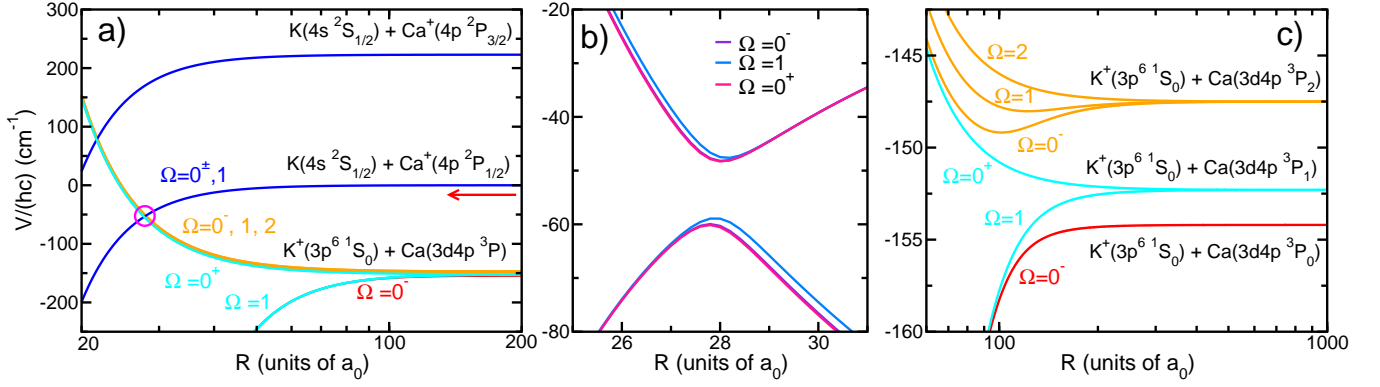


FIG. 8. Long-range adiabatic potential energy curves with  $\Omega = 0^\pm, 1$ , and 2 as functions of the atom-ion separation  $R$ . Panels a) and c) have been computed without the charge-exchange-inducing coupling. Panel (b) shows avoided crossings among adiabatic potentials due to the charge-exchange-inducing coupling near  $R = 28a_0$ . The zero of energy in all panels is located at the  $K(4s\ ^2S_{1/2}) + Ca^+(4p\ ^2P_{1/2})$  entrance channel (red arrow in panel a).

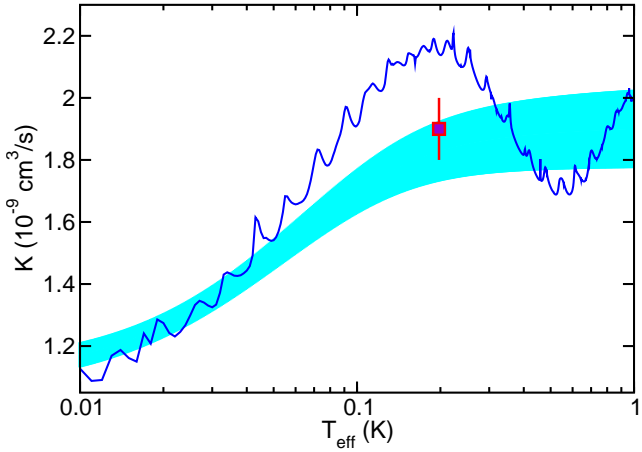


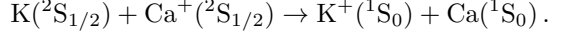
FIG. 9.  $K + Ca^+ \rightarrow K^+ + Ca$  charge-exchange rate coefficients in the presence of the  $Ca^+$ -ion cooling laser based on coupled-channels calculations as a function of collision energy  $E$  or effective temperature  $T_{\text{eff}}$  as defined in the text. The brown curve shows an example of rate coefficient  $K(E)$  as a function of collision energy  $E$ . The cyan colored band corresponds to the thermally-averaged rate coefficient as a function of  $T_{\text{eff}}$ . The width of the band reflects our estimate of the one-standard deviation uncertainty of the coupled channels calculations. Finally, the blue marker with one-standard deviation error bars is our experimentally measured thermally-averaged rate coefficient at  $T_{\text{eff}} = 0.2$  K.

and 1 K. The theoretical rate coefficient is in agreement with the experimental value at  $T_{\text{eff}} = 0.2$  K.

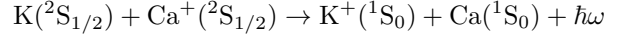
## B. Other charge-exchange pathways in the K and $Ca^+$ system

In this subsection we discuss three other processes that lead to charge exchange between colliding a K atom and a  $Ca^+$  ion. Their rate coefficients turn out to be much

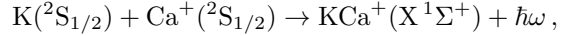
smaller than that for the process described in the previous section. A priori this was not obvious. For completeness, we briefly describe our calculations of these processes. The first process (pathway I) is simply given by the non-radiative process



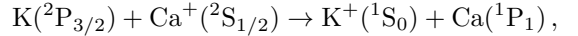
As already schematically shown in Fig. 7a,  $K + Ca^+$  collide on a  $^1\Sigma^+$  and  $^3\Sigma^+$  potential of the  $KCa^+$  molecule. A second process (pathway II) is a radiative process and combines



and



where the colliding atom and ion spontaneously emit photons with energy  $\hbar\omega$ . In the second contribution a molecular ion is formed. Finally, non-radiative pathway III is



enabled by the excitation of potassium atoms to the  $4p\ ^2P_{3/2}$  state due to the absorption of a MOT photon.

Unlike for the calculations in the previous subsection, we have calculated accurate Born-Oppenheimer potential energy curves  $V_s(R)$  for all separations  $R$ . Since the structure of  $KCa^+$  was unknown, we calculated all  $^{2S+1}\Lambda^\pm$  non-relativistic potentials dissociating to the eight energetically-lowest asymptotes of  $K + Ca^+$  and  $K^+ + Ca$ , using a multi-reference configuration-interaction (MRCI) method within the MOLPRO program package [42]. In addition, we required the non-adiabatic coupling function  $Q_{s,s'}(R) = \langle \psi_s; R | d/dR | \psi_{s'}; R \rangle$  and electronic transition dipole moment  $d_{ss',e}(R) = \langle \psi_s; R | \hat{d} | \psi_{s'}; R \rangle$  between the two energetically-lowest  $^1\Sigma^+$  states, where kets  $|\psi_s; R\rangle$  denote the  $R$ -dependent adiabatic electronic eigen states

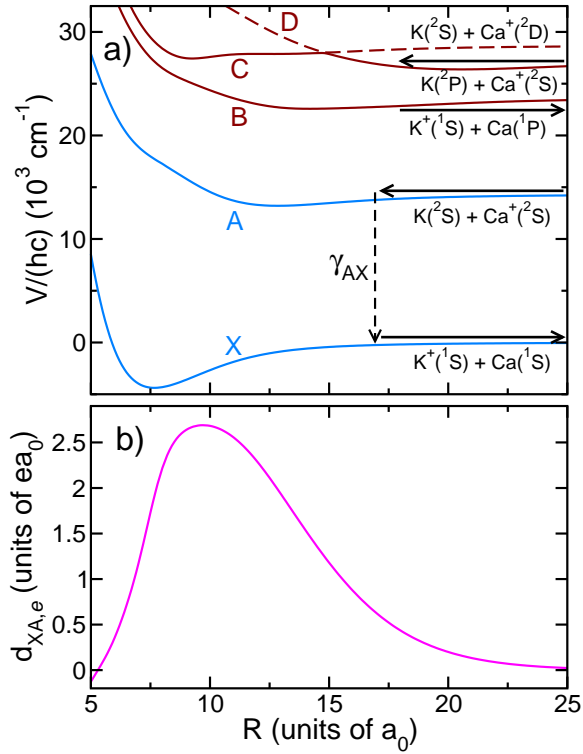


FIG. 10. Panel a) The energetically-lowest five  $^1\Sigma^+$  Born-Oppenheimer potential energy curves, labeled X, A, B, C, and D, as functions of separation  $R$ . The potentials have been computed with a multi-reference configuration-interaction method. The arrows indicate the entrance channels for the three pathways discussed in Sec. III B. The blue curves are relevant for pathways I and III. Red curves are relevant for pathway II. The vertical dashed arrow labeled  $\gamma_{AX}$  represents spontaneous emission from state A to X in pathway III. The zero of energy is at the  $K^+(^1S_0) + Ca(^1S_0)$  limit. Panel b) Electronic transition dipole moment  $d_{XA,e}(R)$  between the ground  $X^1\Sigma^+$  and excited  $A^1\Sigma^+$  adiabatic Born-Oppenheimer states from our MRCI calculations. The potentials and dipole moment for  $R < 5a_0$  are not shown because the entrance channel  $A^1\Sigma^+$  potential is repulsive there and not relevant for the calculation of the rate coefficient.

and  $\hat{d}$  is the electronic dipole operator. Details of these calculations are given in Methods.

Figure 10a) shows the five  $^1\Sigma^+$  Born-Oppenheimer potentials  $V_s(R)$  relevant for the processes described in this subsection. The long-range interaction between an atom in an S-state and an ion in an S-state is isotropic, has  $^1\Sigma^+$  symmetry, and is described by  $-C_4/R^4 - C_6/R^6$ . For the energetically-lowest  $X^1\Sigma^+$  state  $C_4 = 78.5E_h a_0^4$  [43], while for the first-excited  $A^1\Sigma^+$  state  $C_4 = 145.29E_h a_0^4$  [38] and  $C_6 = 3866E_h a_0^6$  [44]. Here,  $E_h$  is the Hartree energy and  $a_0$  is the Bohr radius

### Non-radiative charge exchange by Pathway I

The description of cold charge-exchange collisions by pathway I involves the energetically-lowest two  $^1\Sigma^+$  Born-Oppenheimer potentials, one  $^3\Sigma^+$  potential, the

non-adiabatic coupling between the two  $^1\Sigma^+$  potential leading to charge exchange, but also the atomic hyperfine interaction of  $^{39}K(4s\ ^2S_{1/2})$  between its electron and nuclear spin. The nuclear spin of  $^{40}Ca^+$  is zero. For obtaining a qualitative estimate of rate coefficients for this pathway we can ignore the atomic hyperfine interaction Hamiltonian and then only account for the spin degeneracies.

With these approximations we can set up coupled-channels equations for charge exchange that includes only the isotropic  $X^1\Sigma^+$  and  $A^1\Sigma^+$  Born-Oppenheimer potentials, which are separated in energy by more than  $hc \times 10^3$  cm $^3$ , using a two-channel diabatic representation that can then be used to solve the coupled-channels equations [40]. That is, we start with the  $R$ -dependent electronic eigenstates  $|\psi_s; R\rangle$  with  $s=X$  or  $A$  for the two corresponding adiabatic Born-Oppenheimer states, respectively, and construct  $R$ -independent diabatic electronic basis functions  $|\phi_i\rangle$  with  $i=1, 2$  based on the unitary transformation

$$\begin{pmatrix} |\phi_1\rangle \\ |\phi_2\rangle \end{pmatrix} = \begin{pmatrix} \cos \theta(R) & -\sin \theta(R) \\ \sin \theta(R) & \cos \theta(R) \end{pmatrix} \begin{pmatrix} |\psi_X; R\rangle \\ |\psi_A; R\rangle \end{pmatrix} \quad (4)$$

with mixing angle  $\theta(R) = \int_R^\infty Q_{X,A}(R')dR'$  and non-adiabatic coupling  $Q_{X,A}(R)$  as obtained by our MRCI calculations. The potential matrix elements  $U_{ij}(R)$  in the diabatic basis  $|\phi_i\rangle$  are then

$$\begin{aligned} U_{11}(R) &= V_X(R) \cos^2 \theta + V_A(R) \sin^2 \theta, \\ U_{22}(R) &= V_X(R) \sin^2 \theta + V_A(R) \cos^2 \theta, \\ U_{12}(R) &= U_{21}(R) = (V_A(R) - V_X(R)) \cos \theta \sin \theta. \end{aligned} \quad (5)$$

Figures 10a) and 11 shows all ingredients and results of the process to create  $R$ -independent electronic wavefunctions. Specifically, the inputs are  $V_X(R)$  and  $V_A(R)$  in Fig. 11a) and  $Q_{X,A}(R)$  in Fig. 11b). The resulting mixing angle is shown in Fig. 11c). Finally, diabatic potentials  $U_{ii}(R)$  and coupling  $U_{12}(R)$  are shown in Fig. 11a) and d), respectively. We immediately note the crossing between the two diabatic potentials  $U_{11}(R)$  and  $U_{22}(R)$  near  $R = 9a_0$  and that  $U_{12}(R)$  near these  $R$  values can be as large as the atomic splitting of order  $hc \times 10^4$  cm $^{-1}$ .

As the diabatic potential matrix elements are isotropic, we can use basis functions  $|\phi_i\rangle Y_{\ell m}(\theta, \varphi)$  with  $i=1$  and 2 to expand the total molecular wavefunction. Here,  $Y_{\ell m}(\theta, \varphi)$  is a spherical harmonic,  $\ell$  is the partial wave or the rotational angular momentum quantum number, and  $m$  is its projection quantum number in the laboratory frame. We then solve two-channel radial coupled-channels equations for each partial wave  $\ell$  and  $m = 0$  by numerically propagation and obtain the partial non-radiative charge-exchange (nrCE) rate coefficients  $K_{\ell m}^{\text{nrCE}}(E)$ . The rate coefficient is the same for each  $m$  and  $E$  is the entrance-channel collision energy. The total rate coefficient is then

$$K_{\text{nrCE}}(E) = v\sigma_{\text{nrCE}}(E) = g \sum_{\ell=0}^{\infty} (2\ell+1) K_{\ell 0}^{\text{nrCE}}(E), \quad (6)$$

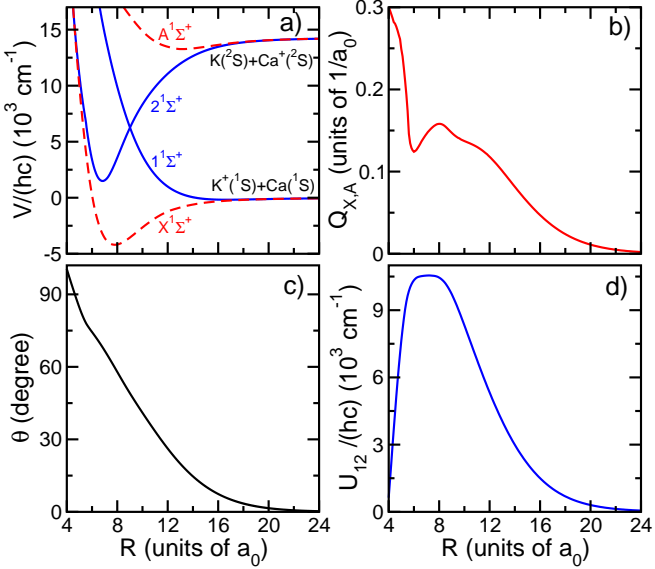


FIG. 11. Diabatic representation of the  $K(^2S_{1/2}) + Ca^+(^2S_{1/2}) \rightarrow K^+(^1S_0) + Ca(^1S_0)$  charge-exchange process. (a) The ground  $X^1\Sigma^+$  and excited  $A^1\Sigma^+$  adiabatic Born-Oppenheimer potentials,  $V_x(R)$  and  $V_a(R)$ , (dashed red lines) and  $1^1\Sigma^+$  and  $2^1\Sigma^+$  diabatic potentials,  $U_{11}(R)$  and  $U_{22}(R)$ , (solid blue lines) as functions of separation  $R$ . (b) the non-adiabatic coupling function  $Q_{x,A}(R)$  between the two  $1^1\Sigma^+$  adiabatic Born-Oppenheimer potentials as a function of  $R$ . Finally, panels c) and d) show mixing angle  $\theta(R)$  and diabatic coupling function  $U_{12}(R)$  as functions of separation  $R$ , respectively.

where  $v = \sqrt{2E/\mu}$  is the relative velocity and  $g = 1/4$  is a statistical probability that accounts for the fact that the entrance threshold  $K(^2S_{1/2}) + Ca^+(^2S_{1/2})$  has singlet and triplet total electron spin channels and that only the singlet  $1^1\Sigma^+$  channel leads to charge exchange.

Figure 12a) shows our non-radiative charge-exchange cross section  $\sigma_{\text{nRCE}}(E)$  for pathway I as a function of collision energies between  $k \times 0.1$  K and  $k \times 100$  K. The sharp resonances are again due to shape resonances of the induction potential from the forty partial waves that contribute significantly to  $\sigma_{\text{nRCE}}(E)$  at  $E/k = 0.2$  K. Thermally averaging as in Sec. III A assuming temperatures  $T_K$  and  $T_{Ca}$  for the potassium atoms and calcium ions, respectively, removes these resonances as shown in Fig. 12b). The rate coefficient is no larger than  $4 \times 10^{-18} \text{ cm}^3/\text{s}$ , eight orders of magnitude smaller than that found in Sec. III A and observed in our experiment.

We finish the discussion of Pathway I by artificially changing the coupling function  $U_{12}(R)$  in order to better understand why our prediction for its charge-exchange rate coefficient is so small. We uniformly scale  $U_{12}(R)$  and have repeated the calculation of  $K_{\text{nRCE}}(E)$  for various scale factors. Figure 13 shows the rate coefficient at a single collision energy as a function of  $U_{12}(R)$  at  $R = 9a_0$ , where the diabatic potentials cross, *i.e.*  $U_{11}(R) = U_{22}(R)$ . The figure also shows a prediction

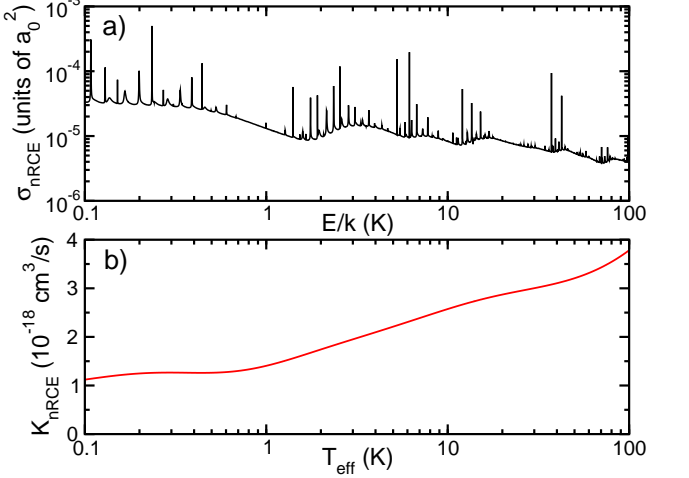


FIG. 12. Panel a) Non-radiative charge-exchange cross section from  $K(^2S_{1/2}) + Ca^+(^2S_{1/2})$  to  $K^+(^1S_0) + Ca(^1S_0)$  as a function of the entrance-channel collision energy. Panel b) Thermalized rate coefficient as a function of temperature based on the cross section shown in panel a).

based on the Landau-Zener curve-crossing model [45, 46] using the coupling strength and value and slopes of the diabatized potentials at the crossing point. Our numerical rate coefficient has a characteristic peaked behavior in good agreement with the Landau-Zener theory. It is largest for  $U_{12}(9a_0)/hc \approx 200 \text{ cm}^{-1}$  and rapidly decreases for both smaller and larger  $U_{12}(9a_0)$ . The rate coefficient based on the Landau-Zener model does not capture the oscillatory behavior of  $K_{\text{nRCE}}(E)$  with coupling strength as quantum interferences are not captured. Clearly, for the physical coupling strength the rate coefficient is almost negligibly small.

## Radiative charge exchange by Pathway II

The description of charge-exchange by spontaneous emission from  $K(^2S_{1/2}) + Ca^+(^2S_{1/2})$  collisions in pathway II involves the same Born-Oppenheimer potentials as in pathway I. In addition to the potentials we require the electronic transition dipole moment between the two energetically-lowest  $1^1\Sigma^+$  adiabatic states,  $d_{XA,e}(R)$  as a function of  $R$ . Figure 10b) shows dipole moment  $d_{XA,e}(R)$  determined by our MRCI calculations. The transition dipole moment is largest near  $R = 10a_0$  close to the inner turning point of the excited  $A^1\Sigma^+$  potential for our cold collision energies. It approaches zero for large separations.

We use the optical potential (OP) approach combined with the distorted-wave Born approximation for the phase shift [47, 48] to calculate the total radiative charge-exchange rate coefficient  $K_{\text{RCE}}(E) = v\sigma_{\text{RCE}}(E)$ . The cross section  $\sigma_{\text{RCE}}(E)$  is then

$$\sigma_{\text{RCE}}(E) = \frac{\pi}{k^2} g \sum_{\ell=0}^{\infty} (2\ell+1) \left\{ 1 - e^{-4\eta_{\ell}(E)} \right\}, \quad (7)$$

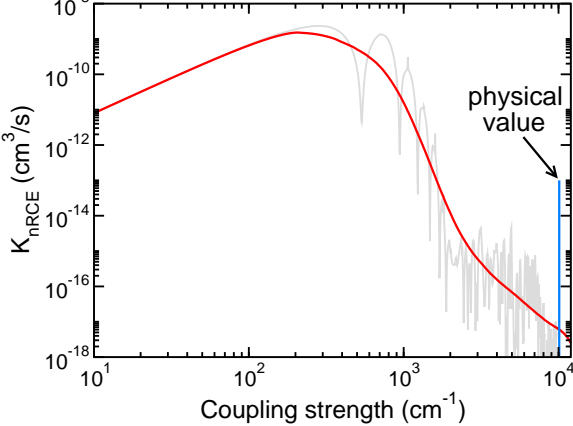


FIG. 13. Non-radiative charge-exchange rate coefficients for  $K(^2S_{1/2}) + Ca^+(^2S_{1/2})$  to  $K(^1S_0) + Ca(^1S_0)$  as functions of diabatic coupling strength  $U_{12}(R)$  at  $R = 9a_0$ , the separation where the two diabatic potentials cross (See Fig. 11a) and d.). The gray curve corresponds to  $K_{nRCE}(E)$  at  $E/k = 0.2$  K, while the red curve corresponds to the rate coefficient based on Landau-Zener theory. The nominal or physical coupling strength is  $U_{12}(9a_0)/hc \approx 9500$  cm<sup>-1</sup> and is indicated by a blue vertical line.

where wavenumber  $k = \sqrt{2\mu E/\hbar^2}$  and the dimensionless quantity.

$$\eta_\ell(E) = \frac{2\pi}{3} \frac{\mu}{k} \alpha^3 \int_0^\infty dR |F_A^{E\ell}(R)|^2 \times |d_{XA,e}(R)|^2 [V_A(R) - V_X(R)]^3, \quad (8)$$

where  $\alpha \approx 1/137$  is the fine-structure constant and  $F_A^{E\ell}(R)$  is a solution of the single-channel radial Schrödinger equation for the  $A^1\Sigma^+$  potential with collision energy  $E$  and partial wave  $\ell$ . In fact,  $F_A^{E\ell}(R) \rightarrow \sqrt{2/\pi} \sin(kR + \delta_{A,\ell}(k))$  for  $R \rightarrow \infty$ , where  $\delta_{A,\ell}(k)$  is the phase shift of the  $A^1\Sigma^+$  potential. In Eq. 8 all quantities are expressed in atomic units. Finally,  $g = 1/4$  is a statistical probability that accounts for the fact that the entrance threshold has singlet and triplet total electron spin channels and that only the singlet  $^1\Sigma^+$  channel leads to radiative transitions.

Figure 14a) shows our radiative charge-exchange cross section  $\sigma_{RCE}(E)$  for pathway II as a function of collision energy. The sharp resonances are again due to shape resonances of the induction potential from the forty partial waves that contribute significantly at  $E/k = 0.2$  K. Thermally averaging assuming temperatures  $T_K$  and  $T_{Ca}$  for the potassium atoms and calcium ions, respectively, removes these resonances as shown in Fig. 14b). The rate coefficient is nearly independent of temperature and no larger than  $4 \times 10^{-14}$  cm<sup>3</sup>/s. This value is much larger than that for the non-radiative process in pathway I, but still four orders of magnitude smaller than observed in

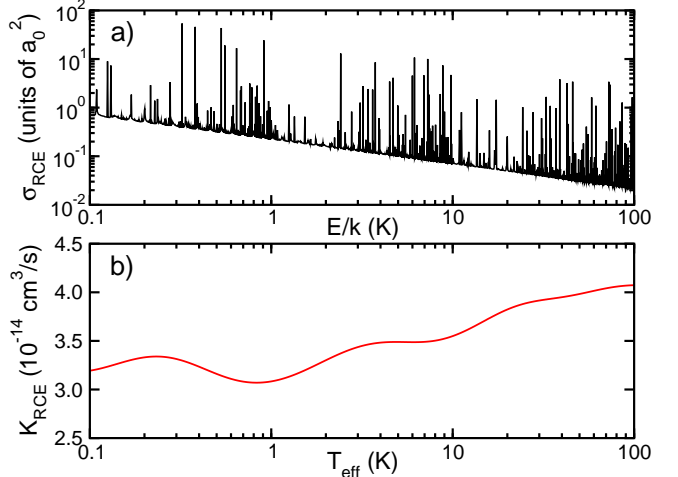


FIG. 14. Panel a: Radiative charge exchange cross-section from  $K(^2S_{1/2}) + Ca^+(^2S_{1/2})$  to  $K(^1S_0) + Ca(^1S_0)$  as a function of the entrance-channel collision energy. Panel b: Thermalized rate coefficient as a function of temperature.

our experiment.

### Non-radiative charge exchange with Pathway III

A potassium atom can be resonantly excited to the 4p  $^2P_{3/2}$  state by the absorption of a photon from the MOT lasers and then react with the calcium ion. That is, the reactants are  $K(^2P)$  and  $Ca^+(^2S)$ . Unlike for Pathway I, more than one product state exists. Several of them have an electronic energy that is a few times  $hc \times 10^3$  cm<sup>-1</sup> lower in energy than that of the reactants and can lead to charge exchange (See figure in Methods.) Based on the results for Pathway I and, in particular, those in Fig. 13, we limit ourselves to the product state  $K(^1S_0) + Ca(^1P_1)$ , which releases the least amount of relative kinetic energy. Even then, a model of charge exchange should include  $\Sigma$  as well as  $\Pi$  molecular states/channels and, as the atomic  $K(^2P)$  configuration is split into  $P_{1/2}$  and  $P_{3/2}$  states, spin-orbit interactions. As our goal is to only obtain an order of magnitude estimate for the rate coefficient it is sufficient to setup a model of charge exchange solely based on the singlet  $^1\Sigma^+$  potentials.

Figure 10a) shows the three relevant highly-excited  $^1\Sigma^+$  Born-Oppenheimer potentials, each dissociating to one of the  $K(^1S_0) + Ca(^1P_1)$ ,  $K(^2P) + Ca(^2S)$ , and  $K(^2S) + Ca(^2D)$  limits. Avoided crossings between the potentials occur at multiple separations. We were, however, unable to compute the non-adiabatic coupling function  $Q_{s,s'}(R)$  among the corresponding  $B^1\Sigma^+$ ,  $C^1\Sigma^+$ , and  $D^1\Sigma^+$  states within the MRCI method. Instead, we resort to further approximations based on the observation that the splitting between the  $C^1\Sigma^+$  and  $D^1\Sigma^+$  potentials at the avoided crossing near  $R = R_{CD} \equiv 15a_0$  is small compared to that of others at smaller separations. In fact, the splitting is much smaller than the energy difference between the  $C^1\Sigma^+$  and  $D^1\Sigma^+$  potentials at

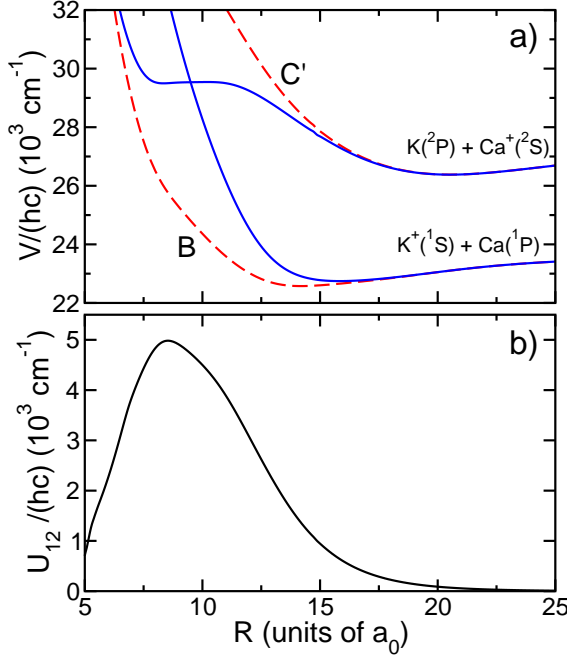


FIG. 15. Potentials and couplings relevant for the non-radiative  $K(^2P) + Ca^+(^2S) \rightarrow K^+(^1S) + Ca(^1P)$  charge-exchange process. (a) The excited  $B^1\Sigma^+$  Born-Oppenheimer potential and partially-diabatized  $C'1\Sigma^+$  potential, as defined in the text, from our MRCI calculations (dashed red lines) as functions of separation  $R$ . The derived diabatic potentials are shown as solid blue curves. (b) Coupling function  $U_{12}(R)$  between the diabatic B and  $C'$  potentials as a function of  $R$ .

$R = R_{CD}$  and that of the  $K(^2P) + Ca^+(^2S)$  reactants and, classically, the crossing can not be accessed. This then implies that to good approximation we can construct a smooth diabatic potential  $U_{ii}(R)$  that closely follows the  $D^1\Sigma^+$  potential for  $R < R_{CD}$  and the  $C^1\Sigma^+$  potential for  $R > R_{CD}$ . We will denote this potential by  $C'1\Sigma^+$ . The other diabatic potential will not be relevant for charge exchange as it dissociates to the  $K(^2S) + Ca(^2D)$  limit. We omit the coupling between these two diabatic potentials.

Figure 15a) shows the  $B^1\Sigma^+$  and  $C'1\Sigma^+$  potentials. The potentials have a broad barely-visible avoided crossing between  $7a_0$  and  $13a_0$  similar in shape to that between the  $X^1\Sigma^+$  and  $A^1\Sigma^+$  potentials for Pathway I. In other words, there exist a weak non-adiabatic coupling between the *adiabatic*  $B^1\Sigma^+$  and  $C'1\Sigma^+$  states and, in fact, we will assume that the mixing angle  $\theta(R)$  between states B and  $C'$  is the same as that between the X and A states shown in Fig. 11c). The derived diabatic potentials  $U_{11}(R)$ ,  $U_{22}(R)$ , and  $U_{12}(R)$  are shown in Figs. 15a) and 15b).

An further analysis of the potentials in Fig. 15 shows that the inner turning point for the reactant collision with relative kinetic energies near  $E/k = 1$  K is around  $18a_0$  for both the adiabatic  $C'1\Sigma^+$  potential and the diabatic potential dissociating to the same limit. Moreover, the

energy of the diabatic potentials at the separation where they cross is higher than that of the  $K(^2P) + Ca^+(^2S)$  reactants. The crossing is not accessible when  $U_{12}(R)$  is either small or large. For the physically-appropriate shape of  $U_{12}(R)$ , the numerically solution of the two coupled channels gives a thermalized rate coefficient of less than  $10^{-18} \text{ cm}^3/\text{s}$  at  $T_{\text{eff}} = 0.2$  K, smaller than that for pathway I.

#### IV. DISCUSSIONS

We have presented our experimental and theoretical investigations of charge exchange interaction between cold  $^{40}\text{Ca}^+$  ions and  $^{39}\text{K}$  atoms. Our theoretical analysis of all possible collision pathways confirms that the reaction occurs via the  $K(^2S_{1/2}) + Ca^+(^2P_{1/2}) \rightarrow K^+(^1S_0) + Ca(3d4p^3P_1) + \hbar\omega$  channel. The experimentally measured charge exchange rate coefficient is in good agreement with our theoretical calculations. In the future, it is possible to induce non-adiabatic transition between the first and the second electronic potentials of  $K\text{Ca}^+$  molecules using an additional high intensity laser. One of the near future goal is to study the effect of this strong interaction on the charge exchange rate.

Over the past decade, hybrid traps proved to be a good platform to study the elastic as well as rich chemical interactions between cold atoms and ions. The next step ahead is to use this platform for attaining the ro-vibrational ground state of molecular ions. The laser cooled atomic ions can efficiently cool the translational degrees of freedom of the molecular ions [49, 50] and the internal states of the molecular ions can be sympathetically cooled using ultra cold atoms. Research towards this goal over the past few years shows promising results [19, 51]. Our next goal involves introducing  $\text{CaH}^+$  molecular ions to the hybrid apparatus and cooling their internal and external degrees of freedom using cold K atoms and  $\text{Ca}^+$  ions. However, the undesired interactions between the atoms, ions and molecular ions[52] as well as unwanted dissociation [53] of the molecular ions in the presence of lasers need to be controlled to achieve this goal. For instance, by manipulating the electronic state population of the  $^{40}\text{Ca}^+$  ions we could control the  $K\text{-Ca}^+$  interaction rate and increase the  $^{40}\text{Ca}^+$  ions lifetime in the presence of K atoms from 2 s to 12 s. Internal state cooling of molecular ions can be observed in the time scale of milliseconds. The already established resolved ro-vibrational spectroscopy measurement of  $\text{CaH}^+$  [54] can be used for the detection of the internal cooling of  $\text{CaH}^+$ . Once prepared in the ground state, the  $\text{CaH}^+$  molecular ions are well suited for the test of fundamental theories such as time variation of the proton to electron mass ratio [55].

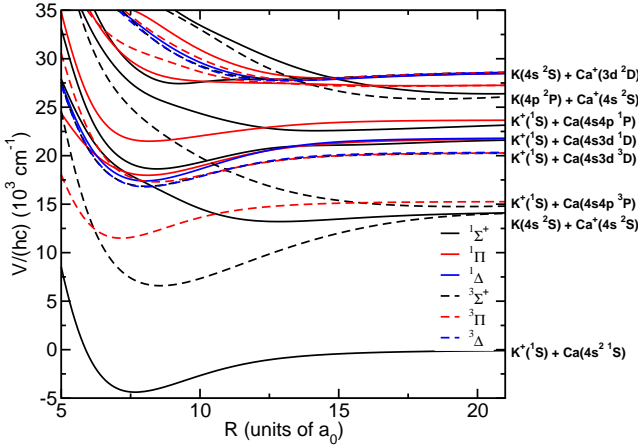


FIG. 16. Non-relativistic  $\text{KCa}^+$  Born-Oppenheimer potential energy curves as functions of separation  $R$ . Potentials of all symmetries dissociating to the lowest eight atomic asymptotes are shown. Asymptotic atomic configurations are given on the right hand side of the graph. The zero of energy is at the  $\text{K}^+(1\text{S}) + \text{Ca}(4s^2 1\text{S})$  limit.

## V. METHODS

We have used the non-relativistic multi-reference configuration interaction (MRCI) method as implemented in the MOLPRO program package [42] to determine adiabatic Born-Oppenheimer potentials, non-adiabatic coupling matrix elements, and electronic transition dipole

moments for the  $\text{KCa}^+$  diatom. The inner-shell electrons for both K and Ca are described by the Stevens-Basch-Krauss-Jansien-Cundari (SBKJC) effective core potentials (ECP) [56], leaving only two valence electrons in the active space. The polarization of the effective cores is modeled via the core polarization potential (CPP) described in Ref. [57]. For the CPP, we use the static dipole polarizabilities of  $\text{K}^+$  and  $\text{Ca}^{2+}$ , which are 5.472 a.u. [58] and 3.522 a.u. [59] respectively. Here, a.u. is an abbreviation for atomic unit. Müller/Meyer type cutoff functions are used with their exponents fitted to the asymptotic energies at large separation  $R$ , which yields the values 0.383 a.u. and 0.465 a.u. for K and Ca, respectively. For K we use the large 7s5p7d2f uncontracted Gaussian basis set from Ref. [60]. For Ca we use the contracted and optimized 9s7p6d/[7s6p6d] basis set from Ref. [61] augmented by three sets of f and one set of g polarization functions [62]. The contractions are specified in the square bracket. The multi-configurational self-consistent field (MCSCF) [63, 64] method is used to obtain configuration state functions (CSF). The MRCI calculation is then performed using a large active space constructed from the CSFs.

Figure 16 shows the results of the MRCI calculations for six non-relativistic symmetries  $^{2S+1}\Lambda^\pm$ . The absolute ground state has  $^1\Sigma^+$  symmetry. Data for this graph is electronically available.

## ACKNOWLEDGMENTS

This work is supported by the MURI Army Research Office Grant W911NF-14-1-0378-P00008 and ARO Grant W911NF-17-1-0071.

---

[1] A. T. Grier, M. Cetina, F. Oručević, and V. Vuletić, Phys. Rev. Lett. **102**, 223201 (2009).

[2] C. Zipkes, S. Palzer, C. Sias, and M. Köhl, Nature **464**, 388 (2010).

[3] S. Schmid, A. Härtter, and J. H. Denschlag, Phys. Rev. Lett. **105**, 133202 (2010).

[4] F. H. J. Hall, M. Aymar, N. Bouloufa-Maafa, O. Dulieu, and S. Willitsch, Phys. Rev. Lett. **107**, 243202 (2011).

[5] W. G. Rellergert, S. T. Sullivan, S. Kotchigova, A. Petrov, K. Chen, S. J. Schowalter, and E. R. Hudson, Phys. Rev. Lett. **107**, 243201 (2011).

[6] A. Härtter, A. Krückow, A. Brunner, W. Schnitzler, S. Schmid, and J. H. Denschlag, Phys. Rev. Lett. **109**, 123201 (2012).

[7] K. Ravi, S. Lee, A. Sharma, G. Werth, and S. A. Rangwala, Nat. Commun. **3**, 1126 (2012).

[8] I. Sivarajah, D. S. Goodman, J. E. Wells, F. A. Narducci, and W. W. Smith, Phys. Rev. A **86**, 063419 (2012).

[9] T. Ray, S. Jyothi, N. B. Ram, and S. A. Rangwala, Appl. Phys. B **114**, 267 (2014).

[10] D. S. Goodman, J. E. Wells, J. M. Kwolek, R. Blümel, F. A. Narducci, and W. W. Smith, Phys. Rev. A **91**, 012709 (2015).

[11] Z. Meir, T. Sikorsky, R. Ben-shlomi, N. Akerman, Y. Dalal, and R. Ozeri, Phys. Rev. Lett. **117**, 243401 (2016).

[12] R. Saito, S. Haze, M. Sasakawa, R. Nakai, M. Raoult, H. Da Silva, O. Dulieu, and T. Mukaiyama, Phys. Rev. A **95**, 032709 (2017).

[13] J. Joger, H. Fürst, N. Ewald, T. Feldker, M. Tomza, and R. Gerritsma, Phys. Rev. A **96**, 030703 (2017).

[14] T. Sikorsky, Z. Meir, R. Ben-shlomi, N. Akerman, and R. Ozeri, Nat. Commun. **9**, 920 (2018).

[15] J. M. Kwolek, D. S. Goodman, B. Slayton, R. Blümel, J. E. Wells, F. A. Narducci, and W. W. Smith, Phys. Rev. A **99**, 052703 (2019).

[16] M. Tomza, K. Jachymski, R. Gerritsma, A. Negretti, T. Calarco, Z. Idziaszek, and P. S. Julienne, Rev. Mod. Phys. **91**, 035001 (2019).

[17] F. H. J. Hall and S. Willitsch, Phys. Rev. Lett. **109**, 233202 (2012).

[18] J. Deiglmayr, A. Göritz, T. Best, M. Weidemüller, and R. Wester, Phys. Rev. A **86**, 043438 (2012).

[19] W. G. Rellergert, S. T. Sullivan, S. J. Schowalter, S. Kotchigova, K. Chen, and E. R. Hudson, Nature **495**, 490 (2013).

[20] P. Staanum, I. S. Jensen, R. G. Martinussen, D. Voigt, and M. Drewsen, Phys. Rev. A **69**, 032503 (2004).

[21] L. Ratschbacher, C. Zipkes, C. Sias, and M. Köhl, Nat.

Phys. **8**, 649 (2012).

[22] R. Ben-Shlomi, R. Vexiau, Z. Meir, T. Sikorsky, N. Akerman, M. Pinkas, O. Dulieu, and R. Ozeri, arXiv preprint arXiv:1907.06736 (2019).

[23] M. Mills, P. Puri, M. Li, S. J. Schowalter, A. Dunning, C. Schneider, S. Kotochigova, and E. R. Hudson, Phys. Rev. Lett. **122**, 233401 (2019).

[24] M. Li, M. Mills, P. Puri, A. Petrov, E. R. Hudson, and S. Kotochigova, Phys. Rev. A **99**, 062706 (2019).

[25] P. Puri, M. Mills, I. Simbotin, J. A. Montgomery, R. Côté, C. Schneider, A. G. Suits, and E. R. Hudson, Nat. Chem. **11**, 615 (2019).

[26] A. D. Dörfler, P. Eberle, D. Koner, M. Tomza, M. Meuwly, and S. Willitsch, Nat. Commun. **10**, 1 (2019).

[27] F. Schmidt-Kaler, S. Gulde, M. Riebe, T. Deuschle, A. Kreuter, G. Lancaster, C. Becher, J. Eschner, H. Häffner, and R. Blatt, J. Phys. B **36**, 623 (2003).

[28] H. Margolis, G. Barwood, G. Huang, H. Klein, S. Lea, K. Szymaniec, and P. Gill, Science **306**, 1355 (2004).

[29] A. Kreuter, C. Becher, G. Lancaster, A. Mundt, C. Russo, H. Häffner, C. Roos, W. Hänsel, F. Schmidt-Kaler, Blatt, and M. S. Safranova, Phys. Rev. A **71**, 032504 (2005).

[30] H. Häffner, C. F. Roos, and R. Blatt, Phys. Rep. **469**, 155 (2008).

[31] R. Blatt and C. F. Roos, Nat. Phys. **8**, 277 (2012).

[32] S. Jyothi, K. N. Egodapitiya, B. Bondurant, Z. Jia, E. Pretzsch, P. Chiappina, G. Shu, and K. R. Brown, Review of Scientific Instruments **90**, 103201 (2019).

[33] S. Bourdeauducq, R. Jördens, Y. Sionneau, D. Nadlinger, D. Slichter, S. Mackenzie, Z. Smith, P. K, M. Weber, F. Held, and D. Leibrandt, “m-labs/artiq: 4.0,” (2018).

[34] S. Haze, R. Saito, M. Fujinaga, and T. Mukaiyama, Phys. Rev. A **91**, 032709 (2015).

[35] A. Kramida, Yu. Ralchenko, J. Reader, and and NIST ASD Team, NIST Atomic Spectra Database (ver. 5.5.6), [Online]. Available: <https://physics.nist.gov/asd> [2018, May 7]. National Institute of Standards and Technology, Gaithersburg, MD. (2018).

[36] J. Mitroy, M. S. Safranova, and C. W. Clark, J. Phys. B **43**, 202001 (2010).

[37] J. Koput and K. A. Peterson, J. Phys. Chem. A. **106**, 9595 (2002).

[38] W. F. Holmgren, M. C. Revelle, V. P. A. Lonij, and A. D. Cronin, Phys. Rev. A **81**, 053607 (2010).

[39] Y. Yu and A. Derevianko, At. Data Nucl. Data Tables **119**, 263 (2018).

[40] E. E. Nikitin, in *Springer Handbooks of Atomic, Molecular, and Optical Physics*, edited by G. W. F. Drake (Springer, New York, 2006) Chap. 49, pp. 741–752.

[41] R. G. Gordon, J. Comp. Phys. **51**, 14 (1969).

[42] H.-J. Werner, P. J. Knowles, G. Knizia, F. R. Manby, and M. Schütz, WIREs Comput. Mol. Sci. **2**, 242 (2012).

[43] S. G. Porsev and A. Derevianko, J. Exp. Theor. Phys. **102**, 195 (2006).

[44] J. Kaur, D. K. Nandy, B. Arora, and B. K. Sahoo, Phys. Rev. A **91**, 012705 (2015).

[45] C. Zhu and H. Nakamura, J. Chem. phys. **102**, 7448 (1995).

[46] P. Coveney, M. Child, and A. Bárány, J. Phys. B. **18**, 4557 (1985).

[47] B. Zygelman and A. Dalgarno, Phys. Rev. A **38**, 1877 (1988).

[48] E. R. Sayfutyarova, A. A. Buchachenko, S. A. Yakovleva, and A. K. Belyaev, Phys. Rev. A **87**, 052717 (2013).

[49] N. Kimura, K. Okada, T. Takayanagi, M. Wada, S. Ohtani, and H. A. Schuessler, Phys. Rev. A **83**, 033422 (2011).

[50] R. Rugango, J. E. Goeders, T. H. Dixon, J. M. Gray, N. B. Khanyile, G. Shu, R. J. Clark, and K. R. Brown, New J. Phys. **17**, 035009 (2015).

[51] A. K. Hansen, O. O. Versolato, L. Kłosowski, S. B. Kristensen, A. Gingell, M. Schwarz, A. Windberger, J. Ullrich, J. R. C. López-Urrutia, and M. Drewsen, Nature **508**, 76 (2014).

[52] E. R. Hudson, Phys. Rev. A **79**, 032716 (2009).

[53] S. Jyothi, T. Ray, S. Dutta, A. R. Allouche, R. Vexiau, O. Dulieu, and S. A. Rangwala, Phys. Rev. Lett. **117**, 213002 (2016).

[54] A. T. Calvin, S. Janardan, J. Condoluci, R. Rugango, E. Pretzsch, G. Shu, and K. R. Brown, J. Phys. Chem. A. **122**, 3177 (2018).

[55] S. Schiller and V. Korobov, Phys. Rev. A **71**, 032505 (2005).

[56] W. J. Stevens, M. Krauss, H. Basch, and P. G. Jasien, Can. J. Chem. **70**, 612 (1992).

[57] W. Müller, J. Flesch, and W. Meyer, J. Chem. Phys. **80**, 3297 (1984).

[58] J. N. Wilson and R. M. Curtis, J. Phys. Chem. **74**, 187 (1970).

[59] H. Coker, J. Phys. Chem. **80**, 2078 (1976).

[60] M. Aymar and O. Dulieu, J. Chem. Phys. **122**, 204302 (2005).

[61] E. Czuchaj, M. Krosnicki, and H. Stoll, Mol. Phys. **98**, 419 (2000).

[62] E. Czuchaj, M. Krosnicki, and H. Stoll, Theor. Chem. Acc. **110**, 28 (2003).

[63] H. Werner and P. J. Knowles, J. Chem. Phys. **82**, 5053 (1985).

[64] P. J. Knowles and H.-J. Werner, Chem. Phys. Lett. **115**, 259 (1985).